International Journal of Geo-Information

MDPI

Article

Deep-Learning-Based Evaluation of Rooftop Photovoltaic Deployment in Tianjin, China

Mei Shan [1], Yue Xu [1], Yun Sun [1], Yuan Wang [1,*], Lei Li [2], Zhi Qiao [1] and Jian Zuo [3]

[1] School of Environmental Science and Engineering, Tianjin University, Tianjin 300072, China; shanyx1_@tju.edu.cn (M.S.); 3021005121@tju.edu.cn (Y.X.); yunna@tju.edu.cn (Y.S.); qiaozhi@tju.edu.cn (Z.Q.)
[2] College of Management and Economics, Tianjin University, Tianjin 300072, China; lilei@tju.edu.cn
[3] School of Architecture and Civil Engineering, The University of Adelaide, Adelaide 5005, Australia; jian.zuo@adelaide.edu.au
* Correspondence: wyuan@tju.edu.cn

Abstract: Rooftop photovoltaics (RPVs) are crucial in addressing energy shortages and environmental concerns caused by fossil fuel combustion. To promote the optimal deployment of RPVs in Tianjin, a region with abundant solar resources and dense buildings, this study proposes a framework that integrates building vector data with a deep learning model to extract currently installed RPVs from remote sensing images, and further estimate the development potential of RPVs. A total of 86,363 RPV polygons were extracted, covering an area of 10.34 km^2. More than 70% of these RPVs are concentrated on large and low-rise buildings, and a similar proportion is found in industrial buildings, as these buildings offer favorable installation conditions. Combining solar radiation and construction land development planning, we further determined the potential deployment zone of RPVs covering about 13% of the Tianjin's land area, which represents 31.31 TWh per year of power generation potential. In the future, it is recommended to prioritize RPV installation on large and low-rise buildings or industrial buildings in the potential deployment zone, which could provide higher power generation and contribute significantly to environmental emission reduction goals. The proposed research framework can also be applied to other cities.

Keywords: rooftop photovoltaics; deep learning; remote sensing; installed RPVs; RPV development assessment

Academic Editors: Wolfgang Kainz and Godwin Yeboah

Received: 6 January 2025
Revised: 11 February 2025
Accepted: 19 February 2025
Published: 22 February 2025

Citation: Shan, M.; Xu, Y.; Sun, Y.; Wang, Y.; Li, L.; Qiao, Z.; Zuo, J. Deep-Learning-Based Evaluation of Rooftop Photovoltaic Deployment in Tianjin, China. *ISPRS Int. J. Geo-Inf.* **2025**, *14*, 101. https://doi.org/10.3390/ijgi14030101

1. Introduction

The historical reliance on traditional fossil fuels for economic development and urban expansion has led to energy shortages and environmental issues [1]. In response, there has been a growing emphasis on renewable and clean energy, particularly solar energy. Photovoltaic (PV) technology, efficiently utilizing solar energy for electricity generation, has been growing rapidly, with the global installed capacity increasing from 136 GW in 2013 to 1411 GW in 2023 [2]. Within this growth, rooftop PV (RPV) systems, deployed on various building rooftops, have also been expanded, reaching an installed capacity of 95 GW by 2022 [3]. RPV systems offer a viable solution to the shortage of ground space in highly urbanized and densely populated regions. Additionally, through decentralized and small-scale installations, RPVs can make considerable contributions to power generation and be directly connected to consumers, providing a rapid response to energy demand [4]. To advance the optimal development of RPVs and better understand their

contribution to responding to energy and environmental challenges, it is essential to accurately assess their deployment potential.

Existing studies on the potential assessment of RPVs generally follow a two-step approach: first, by estimating the available installation space, and then calculating the deployment potential by considering factors such as solar radiation and PV conversion efficiency [5,6]. The key distinction among these studies lies in the method used to estimate the available space. For large-scale studies, researchers predominantly rely on empirical regression models to estimate the area of available rooftop space [7–9]. For example, Zhang et al. (2023) used a Random Forest (RF) regression model to estimate rooftop areas and subsequently calculated the available rooftop space in China using a conversion factor that accounted for building geometric typology, shadows, and obstacles [8]. In contrast, small-scale studies primarily utilize deep learning techniques and remote sensing images to identify available building rooftop [10–12]. For instance, Ni et al. (2024) calculated the available rooftop space at the city scale, considering non-shadowing rooftop areas determined by GIS tools and rooftop obstacles identified by DeepLab-v3 CNN model [10]. While these studies consider multiple influencing factors to estimate the available installation space of RPVs, the majority overlook the dynamic changes in the current status of installed RPVs, and the gap between the available installation space of roof and the actual installation space is the key point in evaluating the installation potential of RPVs. The rapid development of RPVs and urbanization space expansion in China may affect the accuracy of potential assessment results. In recent years, China has experienced rapid growth in distributed PV systems (i.e., majority RPVs), with the share rising from 13% in 2016 to 41% in 2023 [13,14]. There is an urgent need for detailed mapping data of installed RPVs. Therefore, we need to first accurately evaluate the current status of RPV installation, and then estimate the gap between future available space and the current situation in order to assess the potential of RPVs.

Regarding the research methods for evaluating the current status of RPV installation, previous studies have primarily focused on utilizing machine learning models to extract installed PVs on building rooftops from remote sensing images (Table A1). For instance, Zech and Ranalli et al. (2020) employed U-Net models with different backbone networks to extract RPVs in Oldenburg, Germany [15], and Jie et al. (2020) utilized multiple deep learning models (e.g., U-Net, SegNet) to identify RPVs in three cities in California, the United States [16]. These studies have mainly concentrated on countries such as Germany, the United States, and Australia. Only a few studies focus on China; for example, Jiang et al. employed a U-Net model to extract RPV data in the Haian county of Jiangsu. Therefore, the case studies of this research method in China also need to be enriched.

Given the considerations above, this study aims to evaluate the installed RPVs based on a deep learning model and assess RPVs' potential for future deployment using the mega city of Tianjin in northern China as an example. Tianjin is a metropolis with a concentrated population, developed industry, and rapid development of RPVs. In Tianjin, distributed PV systems mainly based on RPV installations increased by 1780 MW between 2016 and 2023 [13,14]. The main research content of this paper includes (1) developing a simple and practical framework to extract installed RPVs from remote sensing images based on a deep learning model; and (2) further assessing the development potential of RPVs by considering key factors, such as solar radiation and construction land planning. This research not only facilitates dynamic monitoring of the RPVs' current status, but also provides valuable insights for policymakers to reasonably plan future RPV deployment.

2. Data and Methods

2.1. Study Area

The study area for this research is Tianjin municipality, situated in the North China Plain and bordering the Bohai Sea. Tianjin enjoys abundant sunlight, with an annual average solar radiation of approximately 5256 MJ/m^2, which is highly favorable for the development of RPV systems. Over the past decade, Tianjin has witnessed a rapid increase in the installed capacity of RPVs. Currently, Tianjin's ambitious renewable energy targets are evident in its "14th Five-Year Plan" for renewable energy development, which outlines a goal to increase solar PV capacity to 5600 MW by 2025 [17]. For RPVs, Tianjin has been actively responding to the national policy "Notice on carrying out the pilot work of rooftop distributed photovoltaic development in the whole district" [18] by launching comprehensive RPV deployment projects in four districts. Additionally, Tianjin is promoting PV installation on new public buildings and factories, aiming for a 50% coverage rate by 2025 [19]. Based on the considerations above, this study strategically selects Tianjin as the research area.

2.2. Data Source

Remote sensing images serve as the primary data for extracting solar PV, with commonly utilized datasets including the Landsat series (15 m/pixel or 30 m/pixel) and the Sentinel series (10 m/pixel or finer). These datasets are freely accessible online but are limited by relatively lower spatial resolutions. Higher-resolution imagery, available from commercial satellites like Spot-6/7 (1.5 m/pixel or finer), Gaofen-2 (0.8–1 m/pixel or 4 m/pixel), and the Google Static Maps API (0.15 m/pixel), offers improved detail but cannot be freely collected [20]. To enhance the generalizability and adaptability of the proposed framework, Google Earth images were selected as the primary input for the deep learning model. Google Earth, an open-source platform, provides extensive global coverage at varying spatial resolutions (0.15–15 m/pixel). In this study, images were acquired within the Tianjin region from 2018 to 2023, featuring a resolution of 0.3 m/pixel.

Additionally, solar radiation data were sourced from WorldClim's historical climate data with a spatial resolution of 1 km [21]. Land use planning data were derived from the General Planning of Land Space of Tianjin report [22]. Other data were obtained from previous studies. Specifically, the building vector data include 280 million buildings in East Asia identified by deep learning from remote sensing images [23]. Local Climate Zones (LCZ) data represent global coverage for 2018 with a spatial resolution of 100 m, encompassing 10 building types and 7 natural land cover types [24]. Building functions include residential, commercial, industrial, administrative and public services, transportation, and parks and green spaces, with parks and green spaces considered unsuitable for RPVs' deployment [25].

2.3. Methodology

The proposed framework for RPVs' extraction and potential analysis is presented in Figure 1. It consists of three main components: (1) extracting the spatial location and size of installed RPVs from remote sensing images based on the adapted U-Net semantic segmentation model and rooftop vector data; (2) further finding the potential deployment zone considering solar radiation and construction land planning; and (3) estimating the power generation, and the environmental and economic impact of RPVs.

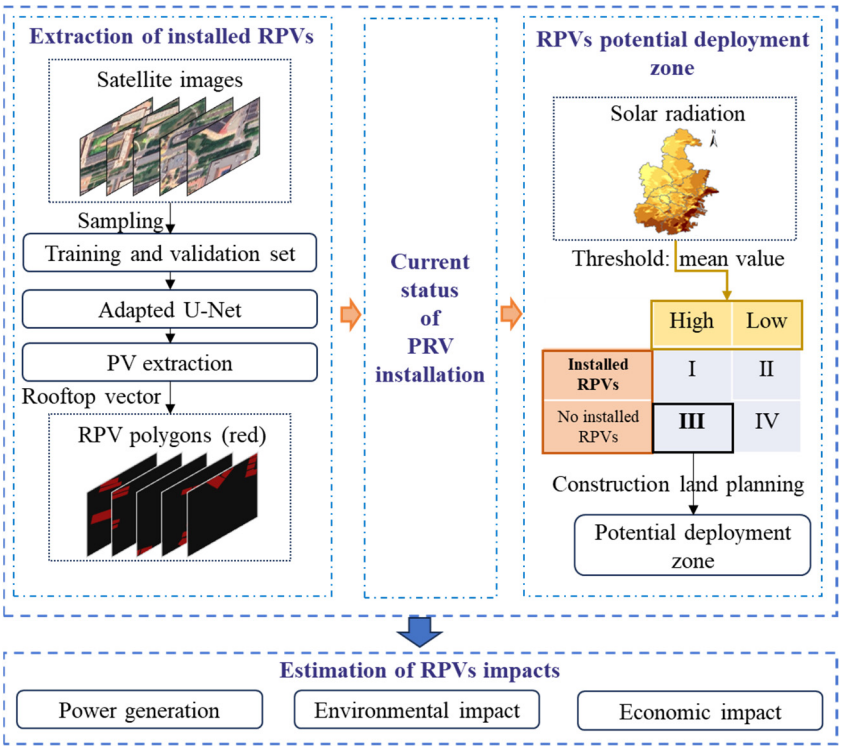

Figure 1. The framework of extraction and potential estimation of rooftop photovoltaic (RPV).

2.3.1. Extraction of Installed RPVs

With the emergence of high-resolution remote sensing images, a variety of machine learning techniques have been employed to extract geospatial and detailed information about installed RPVs from these images. Conventional machine learning algorithms, such as RF classifiers and Support Vector Machines (SVMs), have often been used for RPV classification relying on feature extraction [26,27]. With the rapid development of deep learning, more advanced semantic segmentation models utilizing convolutional neural networks (CNNs) have been adopted to extract RPVs owing to their superior ability to learn image features compared to conventional machine learning algorithms [28,29]. A well-known semantic segmentation model is U-Net, which was originally introduced in 2015 to address medical image segmentation challenges [30]. This model can enhance segmentation performance by combining low-level and high-level features through skip connections, and achieve high-accuracy results with relatively small datasets and shorter training times. Therefore, we utilized the U-Net network as the basic model to extract installed RPVs. By adjusting the basic model's parameter and integrating building vector data, we identified RPVs from remote sensing images as outlined below:

(1) Data preparation and pre-processing

Data preparation. To optimize computational resources and enhance processing efficiency, the remote sensing images were divided into 512 × 512 pixel tiles in TIFF format. Furthermore, we found RPV polygon samples across various districts and building functions in the Google Earth online platform and manually annotated these using the LabelMe tool. A total of 765 tile samples were labeled across Tianjin. The samples were divided into training (60%), validation (20%), and independent test (20%) sets using random sampling (random.sample() function in Python 3.8.0 with a fixed random seed of 0). The validation set was used to monitor model performance during training and guide hyperparameter tuning (e.g., learning rate and batch size). The independent test set was strictly reserved for the final evaluation to ensure an unbiased and reliable assessment of the model's generalization ability.

Data pre-processing. We first conducted shadow detection on the input tiles for the model, followed by data augmentation for those containing shadows, as follows:

Shadow detection: We employed a shadow detection algorithm to identify images with shadowed areas. As the blue (B) and green (G) bands of images contain the most shadow information, the shadow index (SI) defined in Equation (1) was applied [31], and shadows were detected using Otsu's thresholding operation [32].

$$SI = (B - G)/(B + G) \quad (1)$$

Data augmentation: For images containing shadows, data augmentation techniques were utilized to enhance the model's robustness to shadows. These techniques included: (1) Random scaling or warp: the scaling ratio was randomly set between 0.25 and 2. (2) Random flipping: images were flipped with a 50% probability. (3) Random clipping and padding: images were randomly clipped and then pasted onto a new canvas of the target size, with the excess areas filled with gray bars (RGB: 128,128,128). (4) Random color transformation: the hue, saturation and brightness of images were randomly adjusted to make the features of shadowed areas more distinct, thereby improving the model's detection capability. For example, the data augmentation results for an image with shadows are shown in Figure A1.

(2) Adapted U-Net model

To achieve our goals, several meaning modifications were made to the classic U-Net network, resulting in the adapted U-Net model. The architecture of the adapted model is illustrated in Figure 2. The input image was processed through a left contraction path and a right expansion path, ultimately producing an output that classified each pixel as either background (black) or RPV (red). Specifically, in the left contraction path, the input image underwent two consecutive 3 × 3 convolutions, a Rectified Linear Unit (ReLU) activation, and a 2 × 2 max pooling operation. This process was repeated until the feature map resolution was reduced to 32 × 32, with the number of feature channels doubling at each downsampling step, ultimately reaching 1024 channels. In the right expansion path, up-convolutions were applied to double the resolution of the feature map while halving the number of channels. The feature map from the corresponding layer in the left contraction path was concatenated with the upsampled feature map, followed by the application of two 3 × 3 convolutions and ReLU activations. This process was repeated along the expansion path until the feature map resolution matched that of the input image. Finally, a 1 × 1 convolution was performed to produce pixel-level classification results.

In comparison to the classical U-Net, this adapted model incorporates several adjustments, including the following: (1) the tile size was set to 512 × 512 pixels, allowing for greater detail and information retention; (2) zero-padding was applied during convolutional operations to maintain output dimensions consistent with the input image size. Additionally, for the model configuration of adapted U-Net, we first referenced previous studies and selected two of the most commonly used combinations of optimizers, and learning rates [11,29,33]. Specifically, Combination 1 uses Adam optimizer with a learning rate of 0.001, momentum of 0.9 and ReLU activation function; Combination 2 uses SGD optimizer with a learning rate of 0.01, momentum of 0.9 and ReLU activation function. We then systematically tested these combinations. As shown in Table A2, Combination 1 consistently outperformed Combination 2 across all metrics. Therefore, we adopted Combination 1 (Adam optimizer, 1×10^{-4} learning rate, and ReLU activation functions) as our final configuration. Other hyperparameters were tailored to align with the existing computing resources and model requirements. Specifically, we set the batch size to 20 and the epoch number to 100. Furthermore, the SoftMax function was applied to compute the pixel classification probability in the final feature layer, and the binary cross-entropy loss function was utilized as the optimization objective [30,33]. Based on the hyperparameter

configuration above, the adapted U-Net model was implemented with the Pytorch package in PyCharm 2023.2.

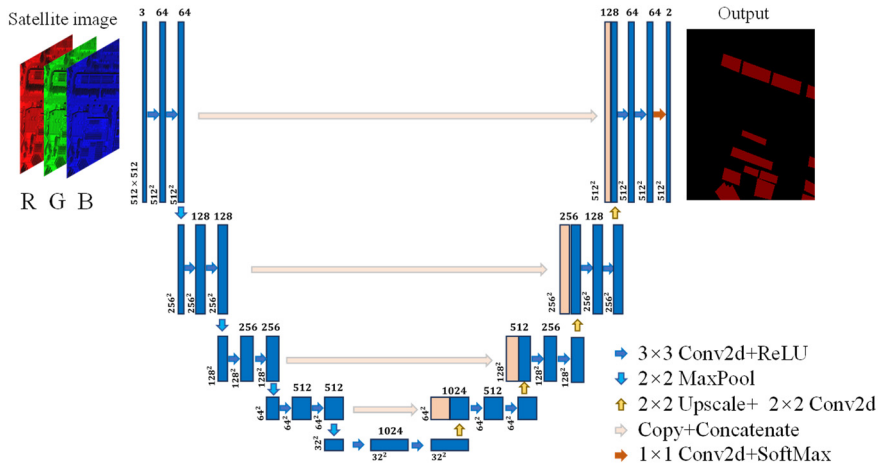

Figure 2. Architecture of adapted U-Net model. Each blue box represents a multi-channel feature map, and each white box indicates a copied feature map. The arrows in different directions denote various operations within the model. The number in the bottom-left corner of each box specifies the size of the feature map, while the number at the top of each box indicates the channel number of the feature map.

(3) Postprocessing

The adapted U-Net model produced a pixel-level classification output of all PVs, presented in raster format for the Tianjin region. Since the objective was to extract the location and area of RPVs, the results required further transformation and processing, as illustrated in Figure 3. First, PV pixels were converted into vector polygons to facilitate the attainment of more details [34]. Based on building vector data, we then filtered the PV polygons outside the building rooftop boundary to obtain RPV polygons. Next, ArcPy geoprocessing tools were used to eliminate internal holes and noise in the RPV polygons, with a noise threshold of 1.6 m², which is the typical size of an individual solar panel [35]. Given that RPV panels are typically rectangular, GIS geometric processing tools were applied to regularize the shape of RPV polygons. Finally, incorrect RPV polygons were manually corrected by visual interpretation and field surveys.

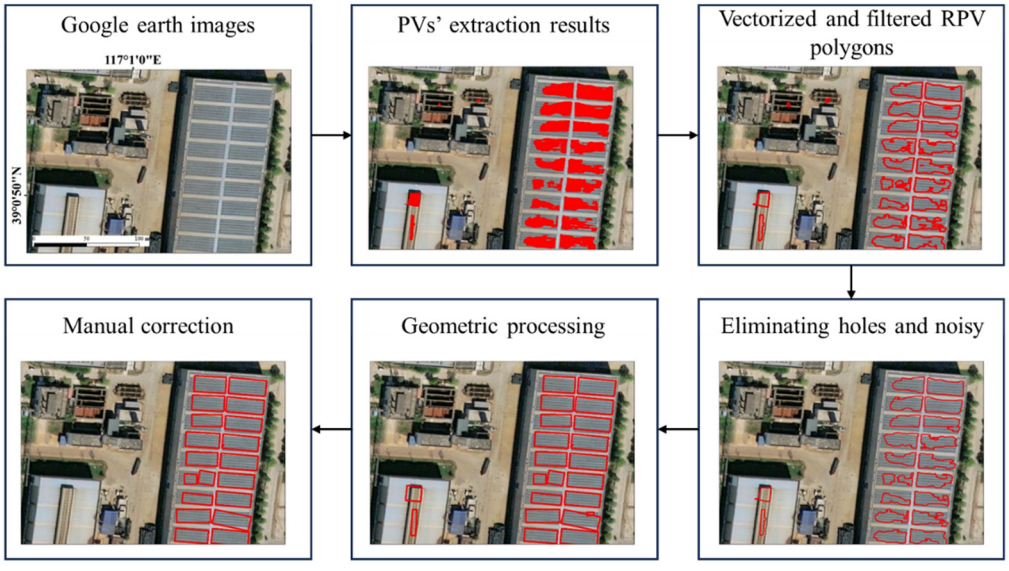

Figure 3. Postprocessing of RPVs. The area shaded in red represents the rasterized PV panels, while the region enclosed by the red lines delineates the vectorized boundaries of the RPV panels.

(4) Model validation and accuracy assessment

To evaluate the accuracy of the revised U-Net model in detecting RPVs, four key metrics were employed, including *Precision*, *Recall*, *F1-score*, and *IoU*. Specifically, *Precision* is the ratio of true-positive predictions to the total number of positive predictions made by the model, which reflects the accuracy of the model in predicting the positive class (Equation (2)). *Recall* is the ratio of true-positive predictions to the total number of actual positive samples (Equation (3)). It indicates the model's ability to detect all the positive samples. Additionally, the *F1-score* is the harmonic mean of Precision and Recall, providing a single score that balances both metrics (Equation (4)). A high *F1-score* indicates that the model has a good balance between Precision and Recall. Finally, *IoU* is a metric used to measure the overlap between the predicted bounding box and the actual bounding box, commonly applied in object detection and image segmentation tasks (Equation (5)). It is calculated as the ratio of the intersection area to the union area of the predicted and actual regions.

$$Precision = TP/(TP + FP) \quad (2)$$

$$Recall = TP/(TP + FN) \quad (3)$$

$$F1 - score = 2 \times Precision \times Recall/(Precision + Recall) \quad (4)$$

$$IoU = TP/(TP + FP + FN) \quad (5)$$

where *TP* means true positive, representing pixels correctly classified as positive (i.e., RPV). *FP* means false positive, expressing pixels incorrectly classified as positive. *TN* means true negative, representing pixels correctly classified as negative (i.e., background). *FN* means false negative, expressing pixels incorrectly classified as negative.

2.3.2. Estimation of RPVs' Impact

The currently installed RPVs and those planned for installation in the potential deployment zone have significant impacts on power generation, environmental emission reduction, and economic benefits. Specifically,

(1) Power generation impact of RPVs

The power generation of installed RPV ($P_{current}$) is the power generated by existing roof-mounted PV, which can be assessed as follows:

$$P_{current} = SA_{current} \times GTI \times CE \times OE \quad (6)$$

where $SA_{current}$ is the area of installed RPVs; *GTI* is the tilted radiation at the optimum angle [36]; *CE* is the conversion efficiency of the PV panels; *OE* represents the overall efficiency for the PV system. Based on previous studies, the range of values for *CE* and *OE* can be found in Table A3. Additionally, based on the rated power (RP) of 200 W/m^2 [8], the capacity of current installed RPVs can be estimated as follows:

$$IC_{current} = SA_{current} \times RP \quad (7)$$

Potential RPV power generation and installed capacity in the potential deployment zone can be calculated as follows:

$$P_{future} = SA_{future} \times CF \times GTI \times CE \times OE \quad (8)$$

$$IC_{future} = SA_{future} \times CF \times RP \quad (9)$$

where SA_{future} is the area of the potential deployment zone; CF represents the conversion factors by adjusting the SA_{future} to the suitable rooftop area of PV, which can be seen in Table A3.

(2) Environmental impact of RPVs

The RPV environmental impact (E) refers to the carbon and air pollutants' emission reduced by the replacement of conventional electricity by RPV power generation, which are usually calculated in terms of emissions generated by an equivalent amount of thermal power generation, as follows:

$$E_{current/future(g)} = P_{current/future} \times E_{F(g)} \quad (10)$$

where g is environmental factors, including carbon, SO_2 and NOx; E_F is the thermoelectric emission factor, which is 0.832 kg kWh^{-1} for carbon, 0.160 g kWh^{-1} for SO_2, and 0.179 g kWh^{-1} for NOx [37].

(3) Economic impact of RPVs

In this study, the RPV economic impact is the electricity bill savings from RPV generation using the net present value (NPV) as a measure. The lifespan (N) of PV modules is 25 years. The net present value (NPV) was employed to assess the economic impact of an RPV over its service life (25 years), which is calculated based on cost and income. The cost includes the initial investment cost and the operation and maintenance cost. The income comprises savings on electricity bills from self-consumption and income from selling surplus power to the grid. Moreover, it is assumed that the degradation rate of the RPV modules introduced only a minor change of around 0.7% per year [38]. Therefore, the economic impact can be expressed as follows:

$$NPV_{current/future} = -C_O \times IC_{current/future} + \sum_{y=1}^{N} \frac{(P_{current/future,y} \times \alpha \times PR_{pur} + P_{current/future,y} \times (1-\alpha) \times PF_{grid} - C_{OM,y \times IC_{current/future}})}{(1+r)^y} \quad (11)$$

where C_O and C_{OM} are the initial investment cost and the operation and maintenance cost of an RPV system, respectively [39]. α is the proportion of self-consumed electricity power [38]. PR_{pur} is the customer-side electricity price from Tianjin Development and Reform Commission, PF_{grid} is the on-grid tariff [40]. r is the social discount rate, which is set to 8%.

3. Results

3.1. Accuracy Evaluation of Adapted U-Net Model

The performance of the adapted U-Net model in extracting installed RPVs was assessed using four widely recognized metrics, Precision, Recall, F1-score, and Intersection over Union (IoU), which were calculated based on the confusion matrix (Table A4). As shown in Figure 4, all four metrics perform well, demonstrating the stability and efficiency of the model. Notably, Recall and Precision exhibit a concentrated and high level of performance, indicating the model's robustness in accurately predicting positive results. The mean values of Recall, Precision, F1 score and IoU were 91%, 93%, 92%, and 85%, respectively. These evaluation results fall within the range estimated by previous studies, which utilized the classic U-Net model or its derived models for PV extraction (Table 1). Meanwhile, the evaluation results from this study outperform most of the previous research. This indicates that the adapted U-Net model is highly effective in accurately detecting solar panels on rooftops.

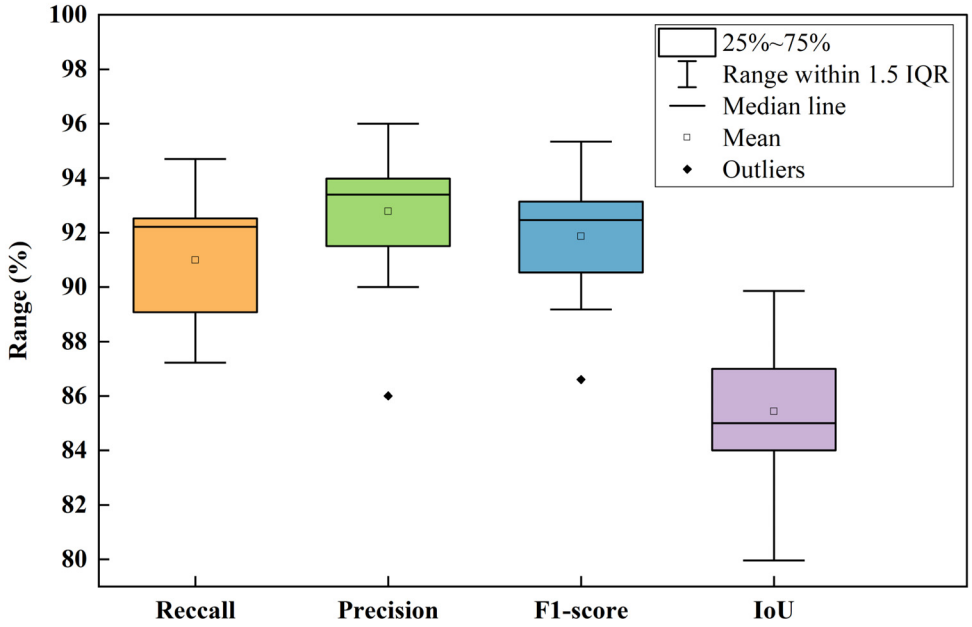

Figure 4. Box plot of evaluation metrics.

Table 1. Accuracy evaluation of adapted U-Net model.

Model	Recall (%)	Precision (%)	F1-Score (%)	IoU (%)	Source
U-Net (ResNet18)	76	83	79	65	[15]
U-Net (ResNet101)	76	86	81	68	
U-Net (ResNet34)	77	84	80	68	
U-Net (ResNet50)	79	84	81	69	
U-Net	/	/	80	64	[41]
U-Net	81	84	83	70	[16]
U-Net + GFM + EDN	83	86	85	74	
U-Net (ResNet50)	89	41	79		[42]
U-Net	90	79	86	79	[43]
U-Net + ResNet50/RNN	90	99	/	90	[28]
U-Net	86	94	90	81	[29]
U-Net (ResNet50) + Transformer	95	97	96	92	
Adapted U-Net	**91**	**93**	**92**	**85**	**This study**

To further assess the accuracy of the adapted U-Net model, its extracted RPV data were compared with two publicly available PV datasets from other studies [29,44], as illustrated in Figure 5. Several representative sites were selected, considering different building functions. The results indicate that the RPVs extracted by the adapted U-Net model are closer to the real PV panels (a1–a4), as more detailed information was captured. Moreover, small-scale PVs on buildings such as residential and public service buildings were also accurately identified (b4 and c4), whereas these PVs were not detected in the studies by Zhang et al. (2022) and Chen et al. (2024) (b2–b3 and c2–c3). This discrepancy can primarily be attributed to the latter studies' focus on detecting large-scale centralized PV systems. Notably, large-scale PV systems, such as the system deployed on the canopy of the Tianjin west railway station, were not detected by the two studies (d2–d3), possibly due to interference from reflective surfaces of adjacent glass. By contrast, the adapted U-Net model effectively identified these PV systems. Overall, the adapted U-Net shows

higher accuracy in identifying RPVs, particularly in detecting small-scale and easily confused RPVs.

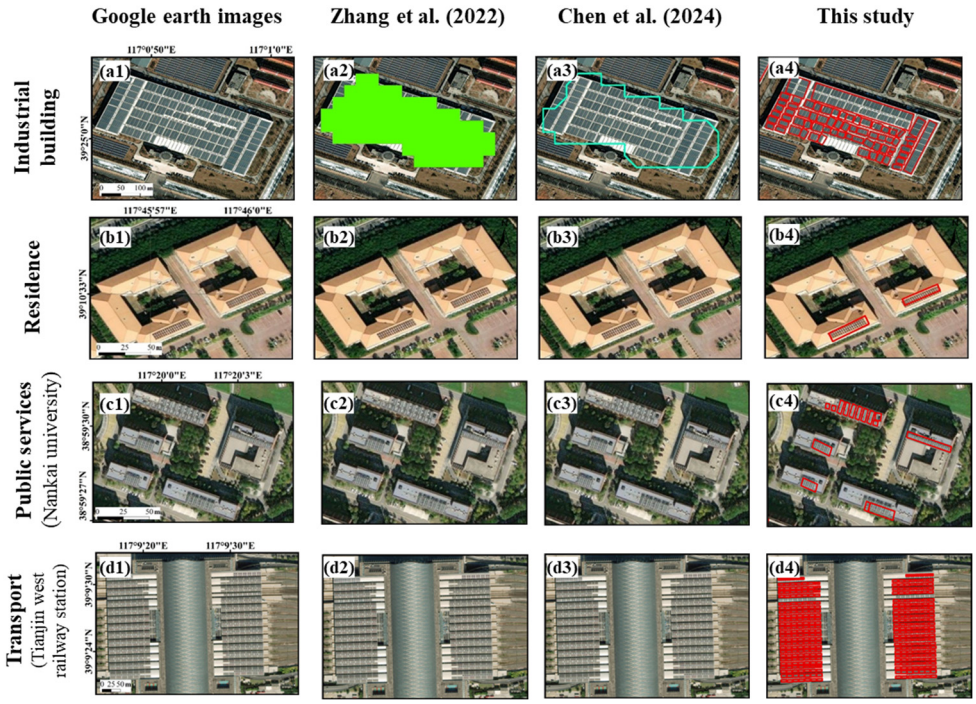

Figure 5. Comparison of RPV extraction results with other studies'. The green shaded area represents the rasterized RPV panels from Zhang et al. (2022) [44], while the regions enclosed by the green and red lines denote the vectorized boundaries of the RPV panels from Chen et al. (2024) [29] and this study, respectively.

3.2. Extraction of Currently Installed RPVs

A total of 86,363 RPV polygons were extracted in Tianjin, covering a total area of 10.34 km^2, which only accounts for approximately 2% of the municipal total building area. This suggests significant potential for further development of rooftop PV systems in Tianjin. Compared with available statistics in 2023, the area of installed RPVs falls within the statistical range for the household and distributed PV installation area (1.16–19.04 km^2), underscoring the rationality of our findings.

The installed RPVs at district level, as illustrated in Figure 6, revealed that DL, BH, and WQ possessed the largest RPV installation areas, measuring 1.77 km^2, 1.54 km^2, and 1.40 km^2, respectively. This trend correlates with their substantial populations (30% of the total) and higher economic output (54% of the total), thereby emphasizing the unique advantage of RPVs in facilitating energy supply proximity to high-demand areas. Notably, DL and BH served as pilot districts for the county-wide distributed photovoltaic projects initiated in 2021, which have experienced rapid development due to favorable policy conditions [18]. In contrast, CC district, despite having the largest population and the second-highest GDP following BH, exhibited the smallest RPV installation area. This limitation is primarily attributable to its smallest geographical extent and high building density, which constrain the rooftop space available for photovoltaic installation [45].

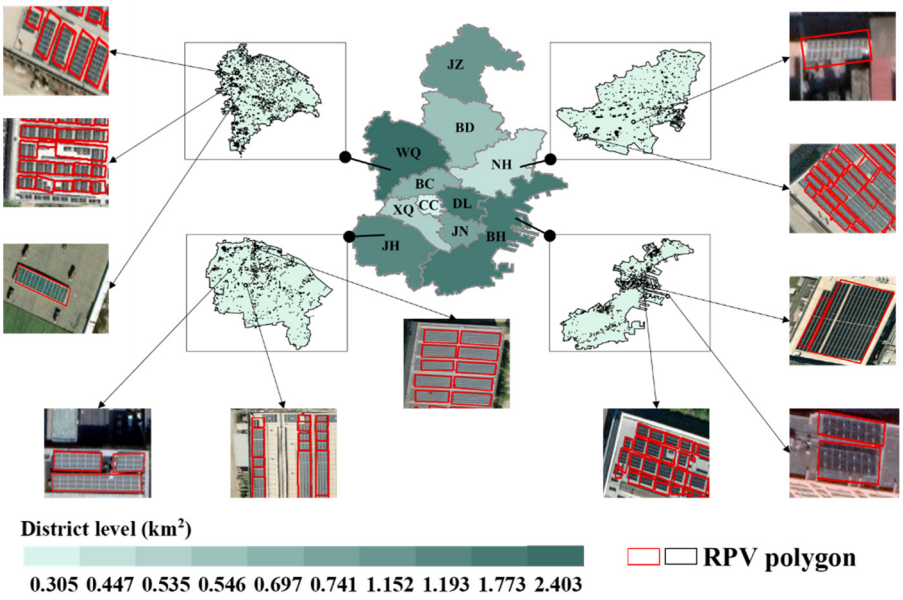

Figure 6. Installed RPV distribution at district and polygon level. The abbreviations of 11 districts in Tianjin are XQ, Xiqing; DL, Dongli; CC, Central city; BC, Beichen; JN, Jinnan; BD, Baodi; WQ, Wuqing; BH, Binhai New Area; NH, Ninghe; JH, Jinghai; JZ, Jizhou.

To investigate the distribution characteristics of RPVs at a finer polygon level, the LCZ map was overlaid with the RPV polygons. The LCZ classification includes 10 built and 7 natural land cover types, with built land cover zones categorized based on building height and building density [24]. As shown in Figure 7a,b, it was observed that most RPV polygons are concentrated in the LCZ8 region, representing over 50% of the total number and total area of polygons. LCZ8 is considered highly suitable for RPV installation due to its low building density, which minimizes the risk of rooftop shading. Additionally, buildings in this zone typically have flat and large roofs with fewer obstacles, providing ample space for photovoltaic systems [46]. A clear trend is also found that RPV polygons are primarily distributed across low-rise buildings (1–3 stories), including LCZ3, LCZ6, LCZ8 and LCZ9. This could be attributed to the simpler roof structures of low-rise buildings, which offer a moderate load-bearing capacity and a lower-risk installation environment, making them ideal for PV installations.

The variation characteristics of RPV polygons under different building functions are also analyzed (Figure 7c). The results show that the majority of RPV polygons are distributed in industrial buildings, accounting for 75% of the total area for polygons. This indicates that industrial buildings are more suitable for PV installations due to their typically larger roof areas and flat roof type, facilitating the efficient layout of solar panels. Moreover, industrial facilities generally have higher electricity demands, making on-site PV systems highly beneficial in reducing electricity costs. RPV polygons in administrative and public service buildings constituted 22% of the total RPV installation quantity, covering 13% of the total installation area. The installation of PV systems on these buildings is not only due to their favorable conditions for installation, such as ample rooftop space, but also serves as a demonstration to enhance public recognition and acceptance of PV power generation [19]. RPVs in residential buildings account for 8% of the total RPV installation area but represent a relatively high installation quantity (17%). Furthermore, a smaller proportion of RPV polygons is observed on commercial and transportation buildings, covering 3% and 2% of the total area, respectively. The irregular roof shapes of these building likely limit the feasibility of PV installation, resulting in lower RPV coverage.

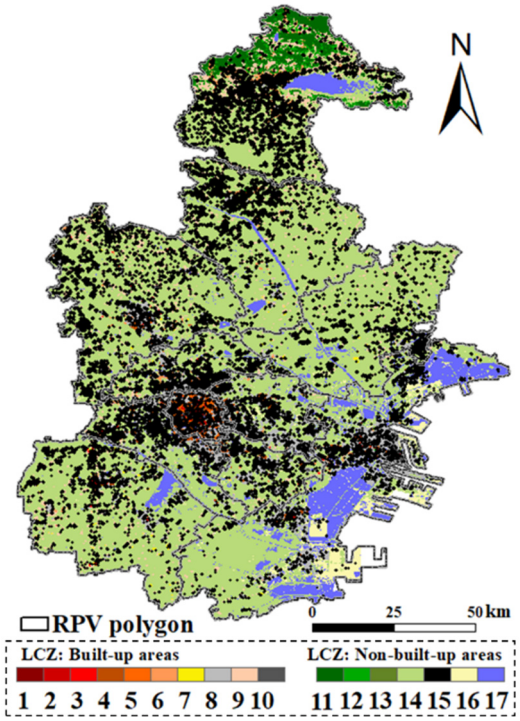

(**a**) Overlay of RPV polygons and local climate zones (LCZ)

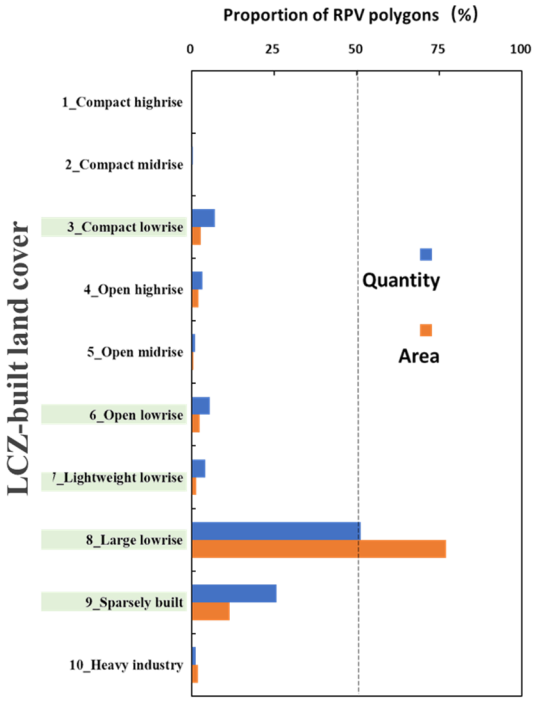

(**b**) Variation in RPV polygons in different LCZ building types

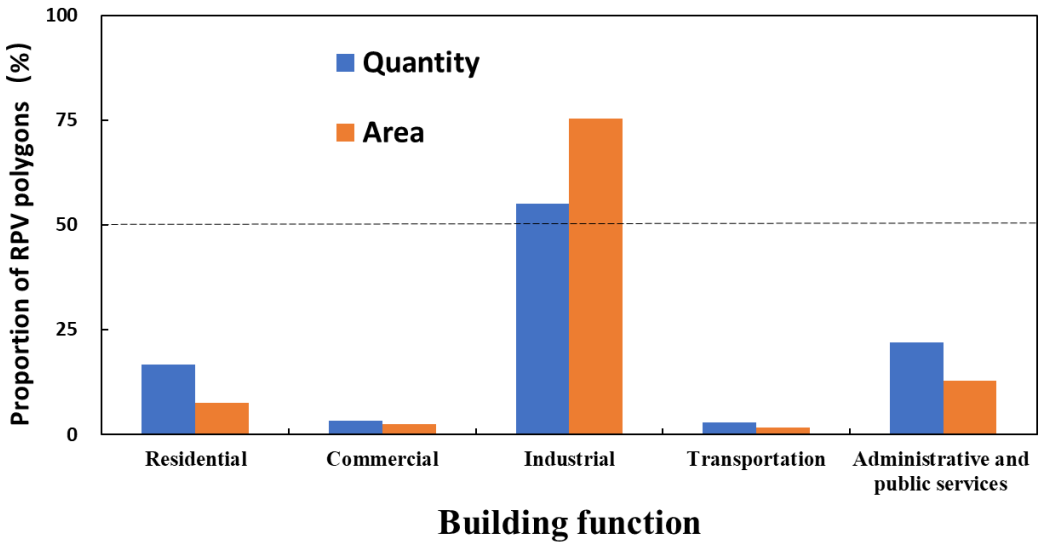

(**c**) Variation in RPV polygons in different building functions

Figure 7. Spatial distribution of RPV polygons. In order, 11–17 represent heavy industry, dense trees, scattered trees, bush, scrub, low plants, bare rock or paved, bare soil or sand, and water.

3.3. Determination of RPV Potential Deployment Zone

Based on the spatial distribution of installed RPVs, the future potential zones for RPV deployment in Tianjin were further determined by considering critical factors such as solar radiation and land spatial development planning. Solar radiation significantly influences the effectiveness of PV systems, as higher solar radiation levels mean more energy output for the same capital input [47]. As shown in Figure 8a, the annual solar radiation in Tianjin generally decreases from east to west. Using the average annual solar radiation as a threshold, Tianjin was classed into high and low solar radiation zones. By overlaying this radiation classification with the presence or absence of installed RPVs, Tianjin was further divided

into four specific zones (Figure 8b). The results reveal that only 30% of installed RPVs are located in the high-solar-radiation zone (Zone I), while the majority are situated in the low-solar-radiation zone (Zone II), indicating that many RPV systems are not operating at optimal generation. This distribution pattern is largely influenced by building spatial locations, with approximately 69% of Tianjin's buildings situated in low-solar-radiation zones.

Based on above consideration, the high-solar-radiation zone without installed RPVs (Zone III) is the preferred zone for future RPV deployment. It is worth noting that urban building design and planning in China adhere to uniform national standard [8]. Therefore, when assessing the RPV potential in China, it is crucial to consider government-led construction land planning as this will determine the future installation spaces for RPVs. In this study, based on the 2021–2035 construction land use planning for Tianjin [22] (Figure 8c), a potential deployment zone of RPVs for the next decade was identified by extracting the overlapping region of construction land and Zone III (Figure 8d). The potential deployment zone is primarily located in the southeast of Tianjin, encompassing districts such as BH, JH and NH, and covering approximately 13% of the municipal land area.

Based on the result analysis in Section 3.2, it can be seen that industrial and LCZ8 buildings characterized by a large size and low density are more suitable for installing RPVs. As shown in Figure 9, the area of LCZ8 buildings is the largest in the potential deployment zone of RPVs, accounting for 77% of the total area of the potential deployment zone. Industrial buildings also have the largest area in the potential deployment zone, accounting for 62%. Therefore, it is recommended to prioritize RPV installation in LCZ8 or industrial buildings in the potential deployment zone, which can maximize the utilization of limited rooftop resources while also reducing installation and maintenance costs. This strategy not only enhances the efficiency of RPV deployment but also supports the overall sustainability and economic feasibility of renewable energy integration in urban settings. It should be noted that this recommendation is made under the assumption that existing buildings will not be demolished and their functions will remain unchanged over the next decade.

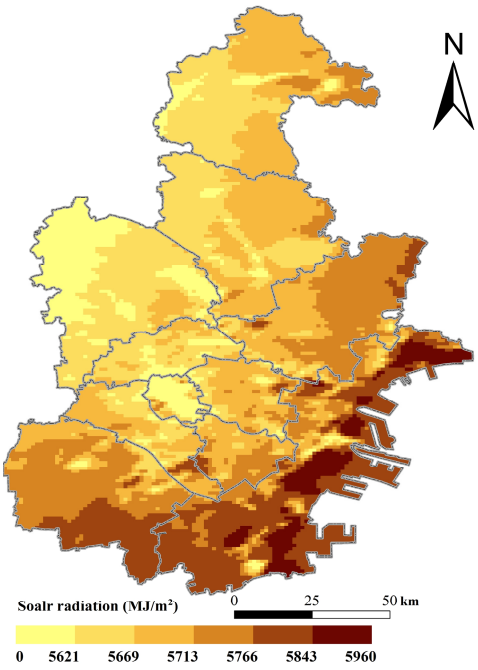

(**a**) Solar radiation

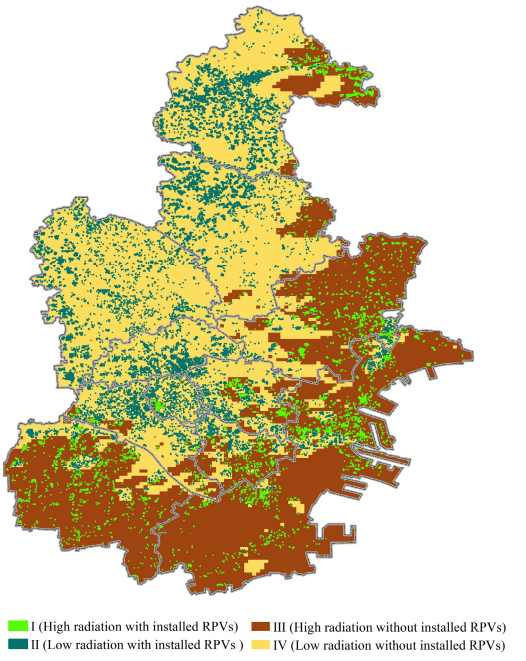

(**b**) Classification map based on current status of installed PRV and solar radiation

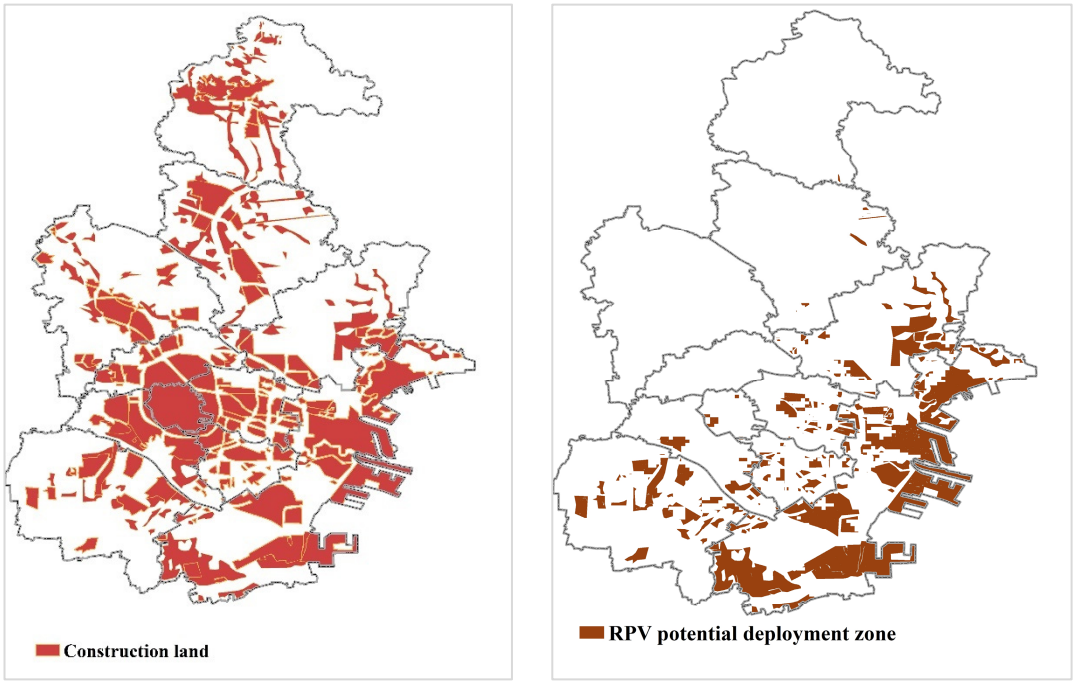

(**c**) Future construction land (**d**) Potential deployment zone of RPVs

Figure 8. Potential deployment zone for RPVs based on solar radiation and land planning.

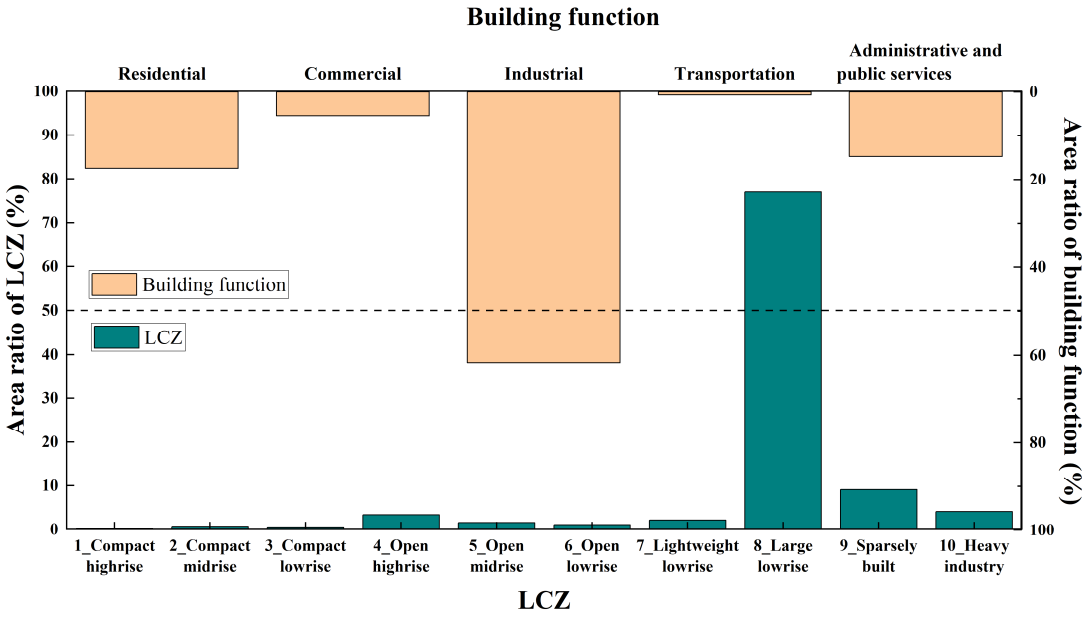

Figure 9. Area proportion of different building functions and LCZ types in potential deployment zone.

4. Discussion

The current and future deployment of RPVs has substantial implications for facilitating energy transition and addressing dual environmental challenges of climate change and air pollution. For currently installed RPVs, according to the solar radiation and efficiency factors of the PV panel and system, it can be estimated that the annual power generation is 1.95–2.95 TWh. This RPV generation could reduce carbon, SO_2, and NOx emissions by 1.62–2.45 MT per year (MT yr^{-1}), 0.31–0.47 KT yr^{-1}, and 0.35–0.53 KT yr^{-1}, respectively.

In the future, if the RPV potential deployment zone is fully equipped with PVs, it can be estimated that the annual RPV power generation could be increased to a minimum of

31.31 TWh, which is equivalent to 41% of Tianjin's thermal power generation in 2023 [48]. This presents a feasible pathway for the transition of traditional energy to renewable energy. Our estimated results of RPV's power generation potential fall within the range of others' estimations (5–51.30 TWh) [5,6,8,49], which validates the reasonableness of our findings. Meanwhile, the emission reductions causing by future RPV generation are 26.05 MT yr^{-1} for carbon, 5.01 and 5.60 KT yr^{-1} for SO_2, and NOx. This highlights the importance of RPV development in addressing environmental challenges, especially in densely populated and highly industrialized cities like Tianjin, which face limited land supply for large-scale PV installations.

The environmental emission reduction potential of the RPV potential deployment zone is compared with other energy solutions and similar studies in other cities. Specifically, (1) comparison with other energy solutions: Due to geographical constraints, the primary renewable energy sources developed in Tianjin include solar photovoltaic (PV), wind power, and biomass energy, which accounted for 58%, 30%, and 12% of the total installed renewable energy capacity in 2020, respectively [50]. To facilitate a meaningful comparison, we evaluated the environmental mitigation potentials of RPV, wind power, and biomass energy (e.g., straw combustion) on a unified basis of annual potential per km^2. The results, presented in Table A5, demonstrate that RPV exhibits significantly higher carbon and air pollution reduction potentials compared to wind power and straw combustion, with wind power outperforming straw combustion. This indicates that solar RPV is a leading energy solution for Tianjin in the future. (2) Comparison with studies in other cities: RPV systems are predominantly deployed in densely built-up areas in eastern China. Therefore, we selected three provincial capital cities—Tianjin (northern China), Nanjing (central-eastern China), and Guangzhou (southern China)—for comparison. These cities exhibit distinct building functions, climate conditions, and energy consumption patterns, as summarized in Table A6. The environmental reduction potentials of RPV installations in these cities are presented in Table A7. The analysis reveals that Nanjing has the highest environmental reduction potential, followed by Tianjin and Guangzhou. This discrepancy may be attributed to the fact that the Nanjing study focused exclusively on residential buildings in the city's five central districts, which offer more available installation space, whereas the studies in Tianjin and Guangzhou encompassed all building types.

Furthermore, RPV power generation can yield significant economic benefits by saving on users' electricity bills. We employed the net present value (NPV) as a metric to assess the economic benefits of RPVs over its service life (25 years). The findings indicate that the installed RPV systems in Tianjin can make profits ranging from CNY 4.31 to 10.57 billion without any subsidies, with an investment payback period of 5 to 9 years. Additionally, the economic benefits from RPV generation in the potential deployment zone are as high as CNY 189.01–694.49 billion. These returns can incentivize users to install PV systems, thereby further promoting environmental emission reductions and the transition to renewable energy.

The RPV potential deployment zone is closely related to the existing infrastructure and population density. Specially, within the potential deployment zone, there is an Ultra-High-Voltage (UHV) substation, as shown in Figure A2a. This substation serves as a critical hub in the North China Power Grid, facilitating the transmission of electricity from western Inner Mongolia to Tianjin. It plays a pivotal role in supporting the power load distribution across the Beijing–Tianjin–Hebei region [51]. The presence of this substation provides a favorable condition for the integration and transmission of photovoltaic-generated electricity. Due to data availability constraints, our discussion is currently limited to the UHV substation. Additionally, the potential deployment zone is well connected to major transportation arteries, including railways, highways, and urban expressways, as illustrated in Figure A2b. This connectivity not only facilitates the transportation and

installation of photovoltaic components but also supports efficient maintenance and operation activities in the future. Finally, the potential deployment zone is densely populated, with the area of high- and medium–high-density population zones accounting for 44% of the total, as depicted in Figure A2c. Consequently, deploying RPV systems in this zone can effectively address the high energy demand driven by the dense population.

There are several limitations to this study. Due to data acquisition constraints, the remote sensing images used to extract installed RPVs were generated at inconsistent times. Consequently, our assessment reflects a cumulative installation quantity over a period. Additionally, confusion has arisen between rooftop PV panels and similar objects, such as glass. Addressing this issue would ideally require both higher-resolution remote sensing images and higher-performance computing devices. However, these conditions are challenging to fully meet. To mitigate such confusion, we conducted as many on-site investigations as possible. Finally, in the determination of the potential deployment zone for RPVs, we focused on key factors affecting future RPV installation, as the available data did not allow us to fully account for all factors. These limitations highlight the need for ongoing research and improved data collection methods to enhance the accuracy of RPV detection and predictions.

5. Conclusions

This study proposes a framework that integrates rooftop vector data into the adapted U-Net model to extract installed RPVs in Tianjin. Based on the extraction results, we further determined the potential deployment zone of RPVs by incorporating key influencing factors. The main research conclusions are as follows: First, a total of 86,363 RPV polygons were extracted from remote sensing images, covering an area of 10.34 km^2. These RPV polygons are primarily distributed in large and low-rise buildings and industrial buildings, as these types of buildings provide optimal installation conditions. Second, the potential deployment zones of RPVs, characterized by high solar radiation and alignment with government land planning, are further determined, which are mainly situated in the southeastern region of Tianjin. The installation of RPVs in these zones will produce about 26.05 TWh of power generation potential while bringing a 26.05 MT yr^{-1} carbon emission reduction and 5.01 and 5.60 KT yr^{-1} SO_2 and NOx emission reductions. Given the conclusions above, in the future, we recommend prioritizing RPV installation on large and low-rise buildings or industrial buildings in the potential deployment zone of RPVs, which could maximize the power generation potential and contribute to achieving carbon neutrality and pollution reduction goals.

Additionally, future research could further explore the topics below.

(1) Addressing deployment challenges in RPV potential zones for industrial and residential buildings (the two largest building categories by area). Residential buildings face (a) limited roof space: the relatively small roof areas of many residential buildings constrain the scale of PV system installation; (b) shading issues: the prevalence of trees and adjacent structures in residential areas creates significant roof shading, adversely affecting PV system efficiency; and (c) aesthetic considerations: homeowners often have specific aesthetic preferences for PV system appearance and installation methods, increasing design and installation complexity. Industrial buildings present (a) high initial investment: the typically large-scale PV installations required for industrial buildings demand substantial upfront capital; (b) energy demand synchronization: the concentrated energy consumption patterns of industrial operations necessitate more sophisticated energy management systems to optimize PV utilization; and (c) structural implications: large-scale PV installations may impact building structures and roof waterproofing, requiring additional engineering design and maintenance considerations.

(2) The impacts of RPVs on urban climate. Specifically, the Weather Research and Forecasting (WRF) model can be used to simulate urban climate changes under three scenarios:

baseline scenario (without RPVs), current RPV installation scenario, and scenario based on the potential deployment zones for RPVs. By comparing these scenarios, we can quantify the effects of RPVs on urban temperature, heat distribution, and other microclimatic variables. The simulations results may reveal that widespread RPV deployment could lead to localized temperature changes due to alterations in surface albedo and heat exchange processes. For instance, RPVs might reduce surface temperatures by shading rooftops but could also contribute to increased ambient temperatures if the absorbed solar energy is re-emitted as heat. These findings would provide critical insights into the trade-offs between renewable energy generation and urban climate regulation. Furthermore, there are potential challenges in integrating the potential deployment zones of RPVs into the WRF model. This requires accurate spatial data on building characteristics and rooftop suitability, as well as careful parameterization of RPVs within the model. Addressing these challenges would require interdisciplinary collaboration and advanced modeling techniques.

Author Contributions: Conceptualization, Yuan Wang, Lei Li, Zhi Qiao and Jian Zuo; Data Curation, Mei Shan and Yue Xu; Formal Analysis, Mei Shan and Yuan Wang; Funding Acquisition, Lei Li and Zhi Qiao; Investigation, Mei Shan, Yue Xu and Yun Sun; Methodology, Mei Shan and Yue Xu; Project Administration, Lei Li and Zhi Qiao; Resources, Mei Shan and Yue Xu; Software, Mei Shan and Yue Xu; Supervision, Lei Li, Zhi Qiao and Jian Zuo; Validation, Mei Shan and Yue Xu; Visualization, Mei Shan and Yuan Wang; Writing—Original Draft, Mei Shan and Yun Sun; Writing—Review and Editing, Mei Shan, Yun Sun, Yuan Wang, Lei Li, Zhi Qiao and Jian Zuo. All authors have read and agreed to the published version of the manuscript.

Funding: This research was funded by the "SDIC Key Project of International (Regional) Cooperation and Exchange Projects of the National Natural Science Foundation of China, grant number: W2412162, funder: Lei Li", and "National Natural Science Foundation of China, grant number: 52270187, funder: Zhi Qiao".

Data Availability Statement: The data that support the findings of this study are openly available, including Google Earth images from Google Earth (https://www.google.com/earth/ (accessed on 9 December 2023)), solar radiation data from WorldClim (https://worldclim.org/data/worldclim21.html (accessed on 9 September 2024)), and Land use planning data from Tianjin Municipal Bureau of Planning and Natural Resources (https://ghhzrzy.tj.gov.cn/zmhd_143/jcyjzj/202109/t20210923_5608995.html (accessed on 9 September 2024)). Other data were obtained from previous studies (Section 2.2).

Acknowledgments: The authors thank the anonymous reviewers and Chenchen Wang for his support during the initial phase.

Conflicts of Interest: The authors declare no conflicts of interest.

Abbreviations

The following abbreviations are used in this manuscript, and the abbreviations of equation variables are in italics.

PV	Photovoltaic
RPV	Rooftop photovoltaic
B	Blue band of images
G	Green band of images
TP	True positive
FP	False positive
TN	Ture negative
FN	False negative
$P_{current}$	Power generation of installed RPV

$SA_{current}$	Area of installed RPVs
GTI	Tilted radiation at optimum angle
CE	Conversion efficiency of the PV panels
OE	Overall efficiency for the PV system
$IC_{current}$	Capacity of current installed RPVs
RP	Rated power of PV panels
P_{future}	RPV power generation in the potential deployment zone
SA_{future}	Area of potential deployment zone
CF	Conversion factors adjusting the SA_{future} to the suitable rooftop area of PV
IC_{future}	Potential installed capacity in the potential deployment zone
$E_{current/future}$	Environmental impact based on RPVs' current status and future potential zone
EF	Thermoelectric emission factor
NPV	Net present value
C_O	Initial investment cost of RPV system
C_{OM}	Operation and maintenance cost of RPV system
α	Proportion of self-consumed electricity power
PR_{pur}	Customer-side electricity price
PF_{grid}	On-grid tariff
r	Social discount rate
LCZ	Local climate zone
IoU	Intersection over Union

Appendix A

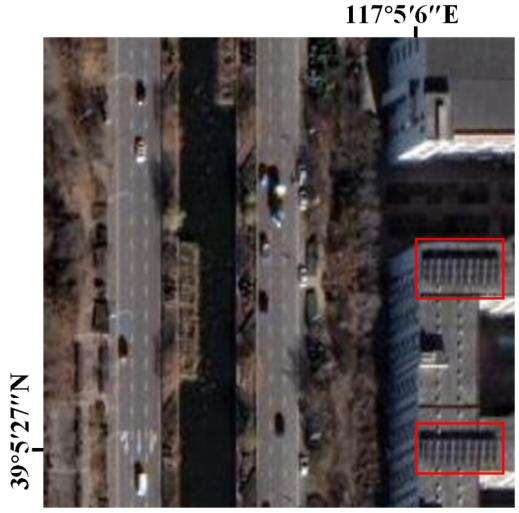

(**a**) Google earth image (the red boxes indicate the RPV panels and their shadows)

(**b**) Flipped vertically

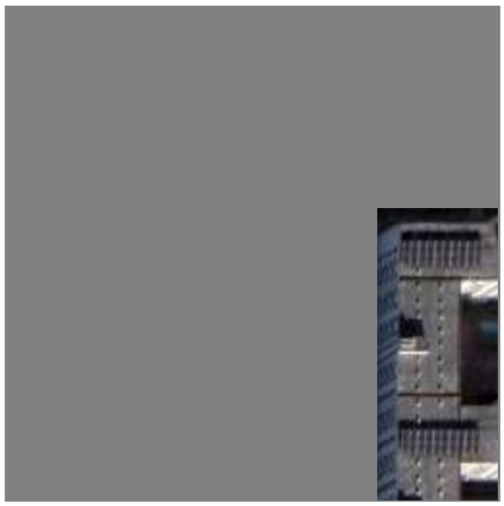

(**c**) Clipped

(**d**) Color transformation

Figure A1. Data augmentation processing.

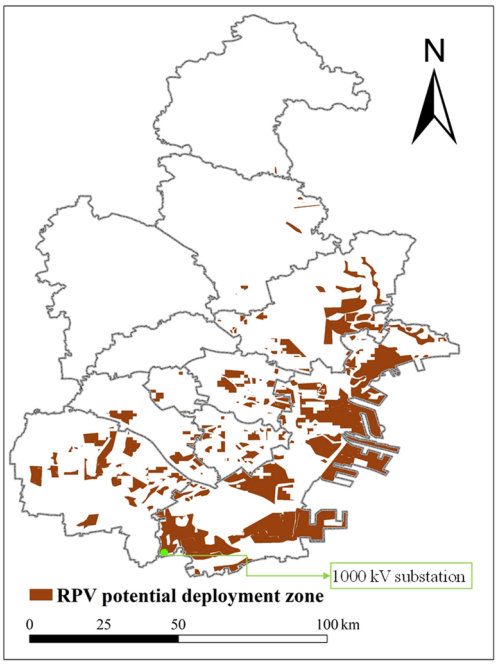

(**a**) 1000 kV substation

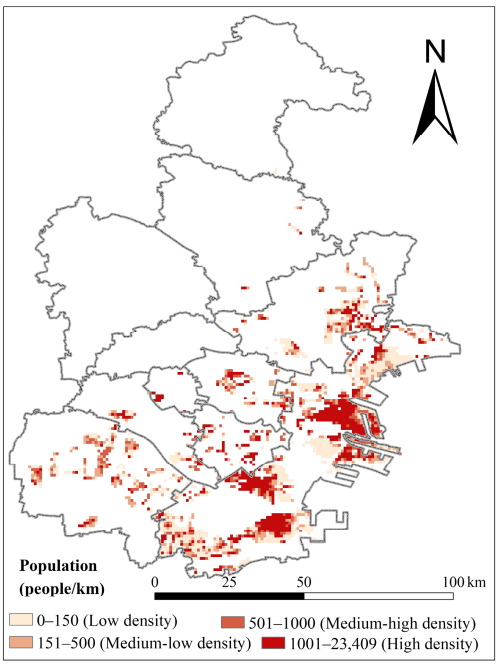

(**b**) Population density

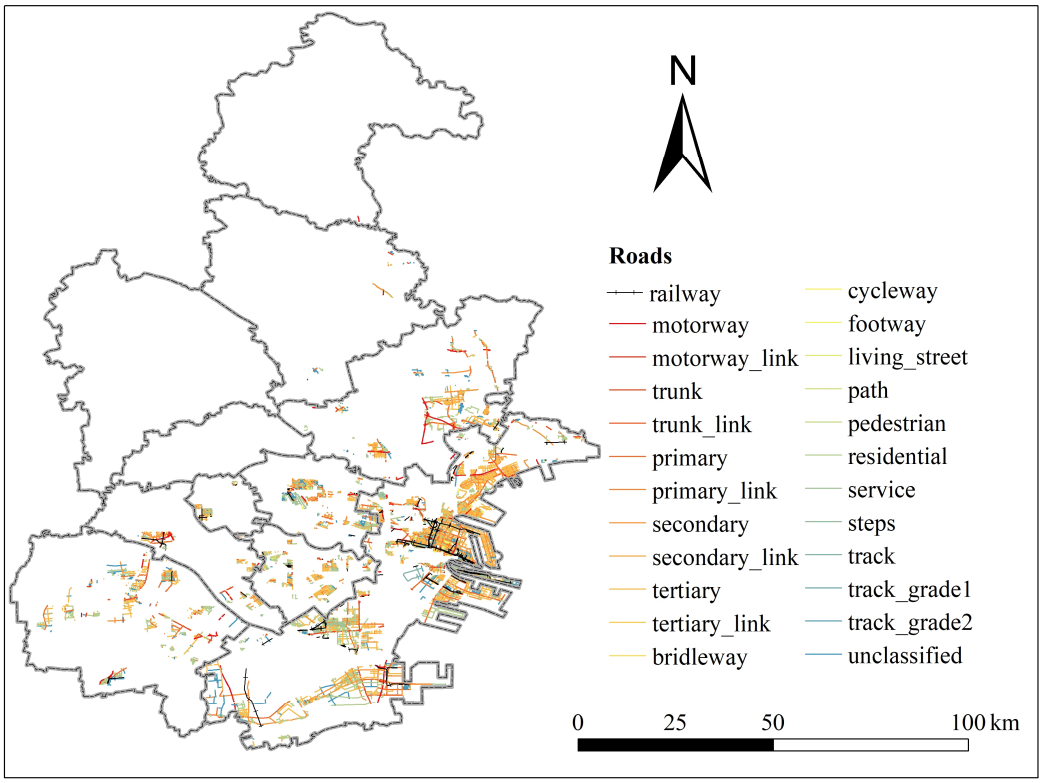

(**c**) Road networks

Figure A2. Existing infrastructure and population in the RPV potential deployment zone: (a) 1000 kV substation (source: [52]), (b) Population density (source: [53]), (**c**) Road networks (source: [54]).

Table A1. Research on small-scale PV extraction based on machine learning.

Sources	Study Areas	PV Type	Models	Precision Evaluation
[41]	Swiss	Rooftop PV	U-Net	IoU: 64%, accuracy: 94%; F1-Score: 80%
[15]	Oldenburg, Germany	Rooftop PV	(1) U-Net (ResNet18); (2) U-Net (ResNet34); (3) U-Net (ResNet50); (4) U-Net (ResNet101)	(1) IoU = 65%, Precision = 83%, Recall = 76%, F1-Score = 79%; (2) IoU = 68%, Precision = 84%, Recall = 77%, F1-Score = 80%; (3) IoU = 69%, Precision = 84%, Recall = 79%, F1-Score = 81%; (4) IoU = 68%, Precision = 86%, Recall = 76%; F1-Score = 81%
[55]	Fresno, Oxnard, Stockton	small-scale residential solar panels	(1) U-Net with trasfer learning; (2) U-Net without trasfer learning; (3) CrossNets (a cross-learning driven U-Net method); (4) Adaptive CrossNets	(1) mIoU: 72.792%, Variance: 1.286×10^{-4}; (2) mIoU: 40.017%, Variance: 1.191×10^{-2}; (3) mIoU: 74.268%, Variance: 2.481×10^{-5}; (4) mIoU: 74.279%, Variance: 1.458×10^{-5}
[16]	Fresno, Stockton, Modesto	Rooftop PV	(1) SegNet (Eff-b1); (2) LinkNet; (3) U-Net; (4) FPN; (5) U-Net + GFM + EDN	(1) IoU: 66.97%, Precision: 83.48%, Recall: 77.20%, F1-Score: 80.22%; (2) IoU: 69.23%, Precision: 83.60%, Recall: 80.11%, F1-Score: 81.82%;

				(3) IoU: 70.28%, Precision: 83.83, Recall: 81.30%, F1-Score: 82.54%; (4) IoU: 71.11%, Precision: 84.79%, Recall: 81.50%, F1-Score: 83.11%; (5) IoU: 73.60%, Precision: 86.17%, Recall: 83.45%, F1-Score: 84.79%
[43]	Hai'an county, China	Rooftop PV	(1) U-Net; (2) RefineNet; (3) DeepLab v3+	(1) IoU: 78.7%, Precision: 78.7%, Recall:90.0%, F1-Score: 86.4%; (2) IoU: 85.9%, Precision: 90.9%, Recall 89.7%, F1-Score: 90.3%; (3) IoU: 86.8%, Precision: 92.8%, Recall 89.4%, F1-Score: 91.1%
[56]	17 cities around the world	Rooftop PV	U-Net: The coding layer of U-Net is replaced with a pre-trained Resnet50. (ResNet50)	Count Recall: 91.90%; Area Recall: 96.25%
[42]	Rwanda	solar home systems (<100 W)	U-Net (ResNet50)	For object: the maximum value of F1-Score is 79%. When the Recall is 89%, the Precision is 41%.

Table A2. Accuracy of different hyperparameter combinations.

	Recall (%)	Precision (%)	F1-Score (%)	IoU (%)
Combination 1	91	93	92	85
Combination 2	80	78	79	76

Table A3. Parameters for calculating the RPV power generation potential.

	Parameter	Low (%)	High (%)	Source
CF	Conversion factor of suitable rooftop	25	59	[5,8,57]
CE	Conversion efficiency of the PV panels	15	20	[8,58,59]
OE	Overall efficiency of the PV system	75	85	[8,59]

Table A4. Confusion matrix for RPV detection.

	TP (%)	TN (%)	FN (%)	FP (%)
Value	19.15	77.57	1.90	1.37

Table A5. Comparison of environmental emission reduction potential of annual RPV power generation in Tianjin with other energy solutions.

	RPV	Wind	Biomass (Agricultural Straw) Lower Calorific Value = 15 MJ/kg	Biomass (Agricultural Straw) Lower Calorific Value = 18 MJ/kg
Power generation potential (GWh/km^2)	19.51	1.58	0.12	0.14
Carbon reduction (MT/km^2)	1.62×10^{-2}	1.31×10^{-3}	9.98×10^{-5}	1.20×10^{-4}
SO_2 reduction (KT/km^2)	3.12×10^{-3}	2.53×10^{-4}	1.92×10^{-5}	2.30×10^{-5}
NOx reduction (KT/km^2)	3.49×10^{-3}	2.83×10^{-4}	2.15×10^{-5}	2.58×10^{-5}

Note: The potential for wind power generation and agricultural straw yield was derived from other research [60,61]. Among these, the agricultural straw yield represents the total amount of straw that could potentially be utilized for energy under the soil ecological retention scenario (low scenario). This yield, when multiplied by the lower heating value and power generation efficiency, equals its power generation capacity. The lower heating value ranges from 15 to 18 MJ/kg [62], and the power generation efficiency is assumed to be 0.3 [63]. The calculation of the environmental emission reduction potential for wind power and straw combustion power generation is the same as that of RPV.

Table A6. Building types, climate conditions and energy consumption patterns in Tianjin, Nanjing and Guangzhou.

City	Main Building Function	Climate Conditions		Energy Consumption Patterns
		Climate	Sunshine Hours	
Tianjin	Residential and industrial Buildings	Temperate Monsoon	2500–2900	Energy consumption is mainly coal-based, accounting for 45% of total energy consumption. Different industrial energy consumption: industry is the main energy-consuming sector, accounting for 77% of total consumption.
Nanjing	Residential, industrial and historical preservation buildings	Subtropical Monsoon	2132	Different industrial energy consumption: industry is the main energy-consuming sector, accounting for 61% of total consumption.
Guangzhou	Residential and commercial buildings	Subtropical Monsoon	1880	Different industrial energy consumption: the service industry is the main energy-consuming sector, accounting for 51% of total consumption.

Note: Data on main building functions are from the Statistical yearbook [48,64]. The sunshine hours of Tianjin are from the 14th Five-Year Plan of Tianjin's renewable energy development [50]; sunshine hours in Nanjing and Guangzhou are from China Meteorological Data Network [8,9]. Energy consumption data of Tianjin, Nanjing and Guangzhou are from local statistical yearbooks [6,10,11].

Table A7. Comparison of environmental emission reduction potential of RPV power generation in Tianjin with other cities.

	Tianjin		Nanjing		Guangzhou	
	Low	High	Low	High	Low	High
Carbon reduction (MT/km^2)	0.016	0.058	1.778	2.074	0.094	0.153
SO_2 reduction (KT/km^2)	0.003	0.011	0.433	0.490	0.018	0.029
NOx reduction (KT/km^2)	0.003	0.012	0.410	0.465	0.020	0.033
Sources	This study		[59]		[65]	

References

1. Cheng, L.; Zhang, F.; Li, S.; Mao, J.; Xu, H.; Ju, W.; Liu, X.; Wu, J.; Min, K.; Zhang, X.; et al. Solar energy potential of urban buildings in 10 cities of China. *Energy* **2020**, *196*, 117038. https://doi.org/10.1016/j.energy.2020.117038.
2. Solar Energy. Available online: https://www.irena.org/Energy-Transition/Technology/Solar-energy (accessed on 10 October 2024).
3. Global Market Outlook for Solar Power 2023–2027. Available online: https://www.solarpowereurope.org/insights/outlooks/global-market-outlook-for-solar-power-2023-2027 (accessed on 9 October 2024).
4. Zhang, Z.; Pu, Y.; Sun, Z.; Qian, Z.; Chen, M. Assessment of rooftop photovoltaic potential considering building functions. *Remote Sens.* **2024**, *16*, 2993. https://doi.org/10.3390/rs16162993.

5. Jiang, H.; Yao, L.; Lu, N.; Qin, J.; Zhang, X.; Liu, T.; Zhang, X.; Zhou, C. Exploring the optimization of rooftop photovoltaic scale and spatial layout under curtailment constraints. *Energy* **2024**, *293*, 130721. https://doi.org/10.1016/j.energy.2024.130721.
6. Wang, L.; Xu, S.; Gong, Y.; Ning, J.; Zhang, X.; Zhao, Y. High resolution photovoltaic power generation potential assessments of rooftop in China. *Energy Rep.* **2022**, *8*, 14545–14553.
7. Joshi, S.; Mittal, S.; Holloway, P.; Shukla, P.R.; Ó Gallachóir, B.; Glynn, J. High resolution global spatiotemporal assessment of rooftop solar photovoltaics potential for renewable electricity generation. *Nat. Commun.* **2021**, *12*, 5738. https://doi.org/10.1038/s41467-021-25720-2.
8. Zhang, Z.; Chen, M.; Zhong, T.; Zhu, R.; Qian, Z.; Zhang, F.; Yang, Y.; Zhang, K.; Santi, P.; Wang, K.; et al. Carbon mitigation potential afforded by rooftop photovoltaic in China. *Nat. Commun.* **2023**, *14*, 2347. https://doi.org/10.1038/s41467-023-38079-3.
9. Gernaat, D.E.H.J.; de Boer, H.; Dammeier, L.C.; van Vuuren, D.P. The role of residential rooftop photovoltaic in long-term energy and climate scenarios. *Appl. Energy* **2020**, *279*, 115705. https://doi.org/10.1016/j.apenergy.2020.115705.
10. Ni, H.; Wang, D.; Zhao, W.; Jiang, W.; Mingze, E.; Huang, C.; Yao, J. Enhancing rooftop solar energy potential evaluation in high-density cities: A Deep Learning and GIS based approach. *Energy Build.* **2024**, *309*, 113743. https://doi.org/10.1016/j.enbuild.2023.113743.
11. Qi, Q.; Zhao, J.; Tan, Z.; Tao, K.; Zhang, X.; Tian, Y. Development assessment of regional rooftop photovoltaics based on remote sensing and deep learning. *Appl. Energy* **2024**, *375*, 124172. https://doi.org/10.1016/j.apenergy.2024.124172.
12. Samhat, A.; Shi, Y.; Zhu, X.; Faour, G.; Ghandour, A. Lebanon solar rooftop potential assessment using buildings segmentation from aerial images. *IEEE J. Sel. Top. Appl. Earth Obs. Remote Sens.* **2022**, *15*, 4909–4918.
13. The Construction of Photovoltaic Power Generation in 2016. Available online: https://www.nea.gov.cn/ (accessed on 9 September 2024).
14. The Construction of Photovoltaic Power Generation in 2023. Available online: https://www.nea.gov.cn/2024-02/28/c_1310765696.htm (accessed on 9 September 2024).
15. Zech, M.; Ranalli, J. Predicting PV areas in aerial images with deep learning. In Proceedings of the 2020 47th IEEE Photovoltaic Specialists Conference (PVSC), Calgary, AB, Canada, 15 June–21 August 2020. https://doi.org/10.1109/pvsc45281.2020.9300636.
16. Jie, Y.; Yue, A.; Liu, S.; Huang, Q.; Chen, J.; Meng, Y.; Deng, Y.; Yu, Z. Photovoltaic power station identification using refined encoder–decoder network with channel attention and chained residual dilated convolutions. *J. Appl. Remote Sens.* **2020**, *14*, 1. https://doi.org/10.1117/1.JRS.14.016506.
17. Outline of the 14th Five-Year Plan for Tianjin's National Economic and Social Development and the Long-Term Goal for 2035. Available online: https://www.tj.gov.cn/zwgk/szfwj/tjsrmzf/202102/t20210208_5353467.html (accessed on 9 September 2024).
18. Pilot List for County Distributed Photovoltaic Development Projects. Available online: https://www.gov.cn/zhengce/zhengceku/2021-09/15/content_5637323.htm (accessed on 9 September 2024).
19. Tianjin Urban and Rural Construction Field Carbon Peak Implementation Plan. Available online: https://zfcxjs.tj.gov.cn/xxgk_70/tzgg/202308/t20230817_6379811.html (accessed on 9 September 2024).
20. Mao, H.; Chen, X.; Luo, Y.; Deng, J.; Tian, Z.; Yu, J.; Xiao, Y.; Fan, J. Advances and prospects on estimating solar photovoltaic installation capacity and potential based on satellite and aerial images. *Renew. Sustain. Energy Rev.* **2023**, *179*, 113276. https://doi.org/10.1016/j.rser.2023.113276.
21. Historical Climate Data. Available online: https://worldclim.org/data/worldclim21.html (accessed on 9 September 2024).
22. General Planning of Land Space of Tianjin (2021–2035). Available online: https://ghhzrzy.tj.gov.cn/zmhd_143/jcyjzj/202109/t20210923_5608995.html (accessed on 9 September 2024).
23. Shi, Q.; Zhu, J.; Liu, Z.; Guo, H.; Gao, S.; Liu, M.; Liu, Z.; Liu, X. The last puzzle of global building footprints—Mapping 280 million buildings in East Asia based on VHR images. *J. Remote Sens.* **2024**, *4*, 0138. https://doi.org/10.34133/remotesensing.0138.
24. Demuzere, M.; Kittner, J.; Martilli, A.; Mills, G.; Moede, C.; Stewart, I.D.; Van Vliet, J.; Bechtel, B. A global map of local climate zones to support earth system modelling and urban-scale environmental science. *Earth Syst. Sci. Data* **2022**, *14*, 3835–3873. https://doi.org/10.5194/essd-14-3835-2022.
25. Gong, P.; Chen, B.; Li, X.; Liu, H.; Wang, J.; Bai, Y.; Chen, J.; Chen, X.; Fang, L.; Feng, S.; et al. Mapping essential urban land use categories in China (EULUC-China): Preliminary results for 2018. *Sci. Bull.* **2020**, *65*, 182–187. https://doi.org/10.1016/j.scib.2019.12.007.
26. Malof, J.M.; Bradbury, K.; Collins, L.M.; Newell, R.G. Automatic detection of solar photovoltaic arrays in high resolution aerial imagery. *Appl. Energy* **2016**, *183*, 229–240. https://doi.org/10.1016/j.apenergy.2016.08.191.

27. Malof, J.M.; Hou, R.; Collins, L.M.; Bradbury, K.; Newell, R. Automatic solar photovoltaic panel detection in satellite imagery. In Proceedings of the 2015 International Conference on Renewable Energy Research and Applications (ICRERA), Palermo, Italy, 22–25 November 2015; pp. 1428–1431.
28. Kruitwagen, L.; Story, K.T.; Friedrich, J.; Byers, L.; Skillman, S.; Hepburn, C. A global inventory of photovoltaic solar energy generating units. *Nature* **2021**, *598*, 604–610. https://doi.org/10.1038/s41586-021-03957-7.
29. Chen, Y.; Zhou, J.; Ge, Y.; Dong, J. Uncovering the rapid expansion of photovoltaic power plants in China from 2010 to 2022 using satellite data and deep learning. *Remote Sens. Environ.* **2024**, *305*, 114100. https://doi.org/10.1016/j.rse.2024.114100.
30. Ronneberger, O.; Fischer, P.; Brox, T. U-Net: Convolutional networks for biomedical image segmentation. In Proceedings of the Medical Image Computing and Computer-Assisted Intervention–MICCAI 2015: 18th International Conference, Munich, Germany, 5–9 October 2015; proceedings, part III; Springer: Berlin/Heidelberg, Germany, 2015; Volume 9351, pp. 234–241. https://doi.org/10.1007/978-3-319-24574-4_28.
31. Muhammed, E.; El-Shazly, A.; Morsy, S. Building rooftop extraction using machine learning algorithms for solar photovoltaic potential estimation. *Sustainability* **2023**, *15*, 11004. https://doi.org/10.3390/su151411004.
32. Joshi, B.; Baluyan, H.; Hinai, A.A.; Woon, W.L. Automatic rooftop detection using a two-stage classification. In Proceedings of the 2014 UKSim-AMSS 16th International Conference on Computer Modelling and Simulation, Cambridge, UK, 26–28 March 2014; pp. 286–291.
33. Sun, T.; Shan, M.; Rong, X.; Yang, X. Estimating the spatial distribution of solar photovoltaic power generation potential on different types of rural rooftops using a deep learning network applied to satellite images. *Appl. Energy* **2022**, *315*, 119025. https://doi.org/10.1016/j.apenergy.2022.119025.
34. Chen, G.; Li, X.; Liu, X.; Chen, Y.; Liang, X.; Leng, J.; Xu, X.; Liao, W.; Qiu, Y.; Wu, Q.; et al. Global projections of future urban land expansion under shared socioeconomic pathways. *Nat. Commun.* **2020**, *11*, 537. https://doi.org/10.1038/s41467-020-14386-x.
35. Solar Photovoltaic Panel Size Guide. Available online: https://www.abpv360.com/a/9599 (accessed on 9 September 2024).
36. Cebecauer, T.; Suri, M. Solar Performance Maps [dataset]. *Solargis* 2020. Available online: https://apps.solargis.com (accessed on 9 September 2024).
37. Annual report on China's electric power industry 2020. Available online: https://cec.org.cn/ (accessed on 9 September 2024).
38. Bai, B.; Wang, Y.; Fang, C.; Xiong, S.; Ma, X. Efficient deployment of solar photovoltaic stations in China: An economic and environmental perspective. *Energy* **2021**, *221*, 119834. https://doi.org/10.1016/j.energy.2021.119834.
39. China PV Industry Development Roadmap. Available online: https://www.chinapv.org.cn/Industry/resource_1380.html (accessed on September 2024).
40. Notice on Matters Related to the On-Grid Tariff Policy of PV Power Generation in 2020. Available online: https://www.ndrc.gov.cn/xxgk/zcfb/tz/202004/t20200402_1225031.html (accessed on 9 September 2024).
41. Castello, R.; Roquette, S.; Esguerra, M.; Guerra, A.; Scartezzini, J. Deep learning in the built environment: Automatic detection of rooftop solar panels using convolutional neural networks. *J. Phys. Conf. Ser.* **2019**, *1343*, 12034. https://doi.org/10.1088/1742-6596/1343/1/012034.
42. Ren, S.; Malof, J.; Fetter, R.; Beach, R.; Rineer, J.; Bradbury, K. Utilizing geospatial data for assessing energy security: Mapping small solar home systems using unmanned aerial vehicles and deep learning. *Isprs Int. J. Geo-Inf.* **2022**, *11*, 222. https://doi.org/10.3390/ijgi11040222.
43. Jiang, H.; Yao, L.; Lu, N.; Qin, J.; Liu, T.; Liu, Y.; Zhou, C. Multi-resolution dataset for photovoltaic panel segmentation from satellite and aerial imagery. *Earth Syst. Sci. Data* **2021**, *13*, 5389–5401. https://doi.org/10.5194/essd-13-5389-2021.
44. Zhang, X.; Xu, M.; Wang, S.; Huang, Y.; Xie, Z. Mapping photovoltaic power plants in China using Landsat, random forest, and Google Earth Engine. *Earth Syst. Sci. Data* **2022**, *14*, 3743–3755. https://doi.org/10.5194/essd-14-3743-2022.
45. Lan, H.; Gou, Z.; Lu, Y. Machine learning approach to understand regional disparity of residential solar adoption in Australia. *Renew. Sust. Energ. Rev.* **2021**, *136*, 110458. https://doi.org/10.1016/j.rser.2020.110458.
46. Chen, Y.; Liu, Y.; Slootweg, M.; Hu, M.; Tukker, A.; Chen, W. Unlocking rooftop potential for sustainable cities: A systematic review. *Front. Eng. Manag.* **2024**. https://doi.org/10.1007/s42524-024-4053-3.
47. Balta-Ozkan, N.; Yildirim, J.; Connor, P.M. Regional distribution of photovoltaic deployment in the UK and its determinants: A spatial econometric approach. *Energy Econ.* **2015**, *51*, 417–429. https://doi.org/10.1016/j.eneco.2015.08.003.
48. Tianjin Statistical Yearbook 2024. Available online: https://stats.tj.gov.cn/nianjian/2024nj/zk/indexch.htm (accessed on 7 February 2025).
49. He, G.; Kammen, D.M. Where, when and how much solar is available? A provincial-scale solar resource assessment for China. Renew. *Energy* **2016**, *85*, 74–82. https://doi.org/10.1016/j.renene.2015.06.027.

50. Tianjin Renewable Energy Development "14th Five-Year Plan". Available online: https://fzgg.tj.gov.cn/zwgk_47325/zcfg_47338/zcwjx/fgwj/202201/t20220127_5791174.html (accessed on 7 February 2025).
51. Tianjin South 1000 kV Substation Will Be Built Within the Year. Available online: https://news.bjx.com.cn/html/20140422/505715.shtml (accessed on 7 February 2025).
52. 2023 Annual Report of State Grid Tianjin Electric Power Company Information Disclosure. Available online: http://www.tj.sgcc.com.cn/html/main/col2792/2024-03/26/20240326143137466720379_1.html (accessed on 6 February 2025).
53. ORNL LandScan Viewer-Oak Ridge National Laboratory. Available online: https://landscan.ornl.gov/ (accessed on 8 February 2025).
54. OpenStreetMap. Available online: https://download.geofabrik.de/ (accessed on 8 February 2025).
55. Zhuang, L.; Zhang, Z.; Wang, L. The automatic segmentation of residential solar panels based on satellite images: A cross learning driven U-Net method. *Appl. Soft Comput.* **2020**, *92*, 106283. https://doi.org/10.1016/j.asoc.2020.106283.
56. Wu, A.N.; Biljecki, F. Roofpedia: Automatic mapping of green and solar roofs for an open roofscape registry and evaluation of urban sustainability. *Landsc. Urban Plan.* **2021**, *214*, 104167. https://doi.org/10.1016/j.landurbplan.2021.104167.
57. Jacobson, M.Z.; Delucchi, M.A.; Bauer, Z.A.F.; Goodman, S.C.; Chapman, W.E.; Cameron, M.A.; Bozonnat, C.; Chobadi, L.; Clonts, H.A.; Enevoldsen, P.; et al. 100% Clean and renewable wind, water, and sunlight all-sector energy roadmaps for 139 countries of the world. *Joule* **2017**, *1*, 108–121. https://doi.org/10.1016/j.joule.2017.07.005.
58. Li, J.; Wang, C.; Guo, J.; Xin, Y.; Zhang, N.; Liu, X.; Feng, K. Promoting sustainable development goals by optimizing city-level solar photovoltaic deployment in China. *Environ. Sci. Technol.* **2024**. https://doi.org/10.1021/acs.est.3c09263.
59. Wang, P.; Yu, P.; Huang, L.; Zhang, Y. An integrated technical, economic, and environmental framework for evaluating the rooftop photovoltaic potential of old residential buildings. *J. Environ. Manag.* **2022**, *317*, 115296. https://doi.org/10.1016/j.jenvman.2022.115296.
60. Zhang, J. *Assessment of Renewable Energy Potentials Based on GIS and RS*; Technische Universität Dortmund: Dortmund, Germany, 2015.
61. Zhu, K.; Liu, Z.; Ou, X.; He, L.; Lin, J. Evaluation of energy-oriented utilization potential of main Chinese crop residues based on soil protection functions. *Chin. J. Eco-Agric.* **2017**, *25*, 276–286. https://doi.org/10.13930/j.cnki.cjea.160671.
62. Introduction of Common Biomass Solid Pellet Fuel Parameters Calorvalue. Available online: http://www.china-nengyuan.com/tech/china-nengyuan_tech_45032.pdf (accessed on 7 February 2025).
63. Biomass Power Generation Technology Summary and Comparative Analysis of Economic Benefits. Available online: https://news.bjx.com.cn/html/20181102/938930.shtml (accessed on 7 February 2025).
64. China County Seat Construction Statistical Yearbook. Available online: https://navi.cnki.net/knavi/detail?p=QRNotohAzjyri1RqHZJaTsF1SQug-eBwO4N_E5_L9nwRVv6AsuhsScJF6v2GXep1m0s1_Cz0ldXfyLtpzI-imXv3gNPIcGzIne0Oq45X_O0=&uniplatform=NZKPT (accessed on 7 February 2025).
65. Pan, D.; Bai, Y.; Chang, M.; Wang, X.; Wang, W. The technical and economic potential of urban rooftop photovoltaic systems for power generation in Guangzhou, China. *Energy Build*. **2022**, *277*, 112591. https://doi.org/10.1016/j.enbuild.2022.112591.